

# Deconvolution of Images Taken with the Suzaku X-ray Imaging Spectrometer

Mutsumi SUGIZAKI<sup>1,2</sup> Tuneyoshi KAMAE<sup>1</sup> and Yoshitomo MAEDA<sup>3</sup>

<sup>1</sup> *Stanford Linear Accelerator Center, 2575 Sand Hill Road, California 94025, USA*  
*kamae@slac.stanford.edu*

<sup>2</sup> *Cosmic Radiation Laboratory, RIKEN, 2-1 Hirosawa, Wako, Saitama 351-0198*  
*sugizaki@crab.riken.jp*

<sup>3</sup> *Institute for Space and Astronautical Science, Japan Aerospace Exploration Agency, Sagamihara, Kanagawa 229-8510*  
*ymaeda@astro.isas.jaxa.jp*

(Received 2007 0; accepted 2008 0)

## Abstract

We present a non-iterative method to deconvolve the spatial response function or the point spread function (PSF) from images taken with the Suzaku X-ray Imaging Spectrometer (XIS). The method is optimized for analyses of extended sources with high photon statistics. Suzaku has four XIS detectors each with its own X-ray CCD and X-Ray Telescope (XRT) and has been providing unique opportunities in spatially-resolved spectroscopic analyses of extended objects. The detectors, however, suffer from broad and position-dependent PSFs with their typical half-power density (HPD) of about  $110''$ . In the authors' view, this shortcoming has been preventing the high collecting area and high spectral resolution of Suzaku to be fully exploited. The present method is intended to recover spatial resolution to  $\sim 15''$  over a dynamic range around 1:100 in the brightness without assuming any source model. Our deconvolution proceeds in two steps: An XIS image is multiplied with the inverse response matrix calculated from its PSF after rebinning CCD pixels to larger-size tiles (typically  $6'' \times 6''$ ); The inverted image is then adaptively smoothed to obtain the final deconvolved image. The PSF is modeled on a ray-tracing program and an observed point-source image. The deconvolution method has been applied to images of Centaurus A, PSR B1509-58 and RCW 89 taken by one XIS (XIS-1). The results have been compared with images obtained with Chandra to conclude that the spatial resolution has been recovered to  $\sim 20''$  down to regions where surface brightness is about 1:50 of the brightest tile in the image. We believe the spatial resolution and the dynamic range can be improved in the future with higher fidelity PSF modeling and higher precision pointing information.

**Key words:** method: data analysis — technique: image processing — X-ray: general

## 1. Introduction

Three X-ray astronomical observatories, Chandra, XMM-Newton, and Suzaku, are operational in orbit now. All have one or more X-ray imaging spectrometers, each made of an X-ray mirror and an X-ray CCD array. Among the three, Suzaku has the second largest effective area at higher energies ( $590 \text{ cm}^2$  at 8 keV) when its four X-ray imaging spectrometers (XISs) are combined, the best energy resolution (FWHM  $\sim 130 \text{ eV}$  at 5.9 keV) and the lowest background rate ( $\sim 1.0 \times 10^{-7} \text{ counts s}^{-1} \text{ keV}^{-1} \text{ arcmin}^{-2} \text{ cm}^{-2}$  at 6 keV) (Mitsuda et al. 2007). However, these advantages are often compromised by its relatively poor spatial resolution. The half power diameter (HPD) of the Chandra, XMM-Newton and Suzaku X-ray imaging spectrometers are about  $1''$ ,  $8''$ , and  $110''$ , respectively. The point spread function (PSF) of the four Suzaku XISs is not only large and complex but depends on the position in the focal plane making analyses of source-rich regions or extended sources difficult (Serlemitsos et al. 2007). Whereas the HPD of the Suzaku X-ray telescopes (XRTs) is large, their PSF has a sharp core with an exponential radial profile of characteristic spread  $\sim 10''$  (Serlemitsos et al. 2007). The pixel size of the XIS CCDs is  $1''.04$  and much smaller than the width of the PSF (Koyama et al. 2007a). If a high number of photons are available, spatial resolution of XIS can be recovered to the PSF core size ( $\simeq 10''$ ). We present here a first attempt to improve spatial resolution of Suzaku XIS by deconvolving the PSF.

In astronomy, many attempts have been made in the past to obtain better spatial information from observed data as reviewed by Starck et al. (2002) and Puetter et al. (2005). Several attempts have been reported for ASCA X-ray images which had a PSF similar to that of Suzaku. White & Buote (2000) employed a maximum-likelihood method to deconvolve images of the Gas Imaging Spectrometer (GIS) aboard ASCA. They reconstructed spatially resolved spectrum by first deconvolving energy-selected images with a maximum-likelihood method and then reassigning individual observed photons to a position in the deconvolved image space with a Monte-Carlo method. Hwang & Gotthelf (1997) applied a Richardson-Lucy method to Solid-state Imaging Spectrometer (SIS) images of a supernova remnant in selected energy bands. In these methods, images are deconvolved by assuming a model of extended emission or a collection of point sources.

Because of the high through-put provided by the four Suzaku XISs, photon statistics does not limit fidelity of image deconvolution for bright targets. The inverse matrix method used in this work can recover the true image if the response matrix is known accurately and if the photon statistics is high in the region of interest. The method has a merit that it does not require any prior model to fit and hence relatively free of systematic bias. It is best suited for

complex extended sources.

Our prime targets are galaxy clusters, pulsar wind nebulae and supernova remnants. The response function of the detector must be modeled accurately and the noise due to Poisson fluctuation must be controlled well to reproduce the image faithfully in typical brightness variation (an order of magnitude) in these extended objects. Since the PSF of Suzaku XIS is complex, the method requires intense labor. Once a procedure is established, however, this method can be set up for automatic deconvolution with minimum human intervention.

The goal of this deconvolution is to recover spatial resolution to  $\sim 15''$  while keeping fidelity in a dynamic range around 1:100 in the brightness. Deconvolution proceeds in two steps: Each XIS image is multiplied with the inverse response matrix calculated from its PSF after rebinning the raw CCD image to larger tiles (typically  $6'' \times 6''$ ). This is required to secure high photon counts in each image elements. The inverted image is then adaptively smoothed to obtain the final deconvolved image.

When this work began, the released XIS images were degraded due to wobbling of satellite pointing (Serlemitsos et al. 2007). We have added one more step to correct for this pointing error by using a bright point source. We have modeled the PSF in two ways: one based on the ray-tracing simulation program developed by the Suzaku team (Ishisaki et al. 2007) and the other by fitting the image of Centaurus A. The two PSFs agree well for XIS-1 but not for the others. For this reason we use only one of the 4 XISs when deconvolving the images of Centaurus A, PSR B1509-58 and RCW 89.

The paper proceeds as follows. We present our image-deconvolution method in section 2. The Suzaku data processing and the correction procedure for the pointing error are described in section 3. The PSF modeling is explained in section 4. We then apply our deconvolution method to XIS-1 images and compare the results with corresponding images of Chandra ACIS in section 5. Conclusions and our future plan are given in section 6.

## 2. Deconvolution by Inverse Response Matrix and Adaptive Smoothing

We here denote an image derived by multiplying an observed image with the inverse response matrix as an “inverted image”. When an “inverted image” is adaptively smoothed, we called it an “deconvolved image.”

### 2.1. Inverse Matrix Method

The relation between an observed image  $d(\vec{x})$  and a true image on the sky  $s(\vec{x})$  is represented by

$$d(\vec{r}) = \int s(\vec{r}') P(\vec{r}'; \vec{r}) d\vec{r}' + n(\vec{r}) \quad (1)$$

where  $P(\vec{r}'; \vec{r})$  is PSF at the source position  $\vec{r}'$  and  $n(\vec{r})$  represents collection of “noises” like Poisson fluctuation in photon counts, instrumental noise, and imperfect PSF modeling.

An observed image taken by a pixelized imager such as a CCD is represented by a finite dimension vector  $\vec{d} = \{d_i\}_{i=1\dots N}$ , where  $N$  is the number of pixels used in the inversion. We combined multiple CCD pixels into a tile to control Poisson fluctuation. The image region contains  $64 \times 64$  tiles and hence  $N = 4096$ .

The discretized version of equation (1) is

$$d_i = \sum_j p_{ij} s_j + n_i \quad (i = 1\dots N), \quad (2)$$

where  $\vec{p}_j = \{p_{ij}\}_{i=1\dots N}$  is the PSF at the  $j$ -th tile,  $\vec{r}_j$ . The response matrix, is then a matrix consisting of  $N$  PSF-vectors and equation (2) becomes

$$\vec{d} = P\vec{s} + \vec{n}, \quad (3)$$

where  $P$  is,

$$P = \{\vec{p}_1 \vec{p}_2 \dots \vec{p}_N\} \quad (4)$$

The inverse response matrix is represented by  $P^{-1}$ . The inverted image  $\vec{s}' = \{s'_i\}_{i=1\dots N}$  is calculated by multiplying the inverse response matrix  $P^{-1}$  (dimension  $N \times N$ ) to a raw image vector  $\vec{d}$  as,

$$\vec{s}' = P^{-1}\vec{d} = P^{-1}(P\vec{s} + \vec{n}) = \vec{s} + P^{-1}\vec{n} \quad (5)$$

When the noise term  $P^{-1}\vec{n}$  is negligible relative to the signal  $\vec{s}$ , the inverted image is a good approximation to the true image. However, this is not true generally. In many cases, the noise term,  $P^{-1}\vec{n}$ , dominates over the signal in the inverted image as described in Starck et al. 2002; Puetter et al. 2005. We control this noise term by adaptive smoothing as will be described in the next subsection.

## 2.2. Adaptive Smoothing of Inverted Image

We employ a technique known as adaptive smoothing to control the noise term in the inverted image while keeping highest spatial resolution compatible with photon statistics. Adaptive smoothing is a generic smoothing method where the spatial resolution is balanced to the signal-to-noise ratio expected for each position in the image (e.g. Lorenz et al. 1993; Huang & Sarazin 1996; Ebeling et al. 2006). It can be optimized to a strategy: we take a uniform significance approach in which the smoothing scale is adjusted so that the smoothed data have a similar signal-to-noise ratio everywhere in the image. This approach has been employed in AKIS (Huang & Sarazin 1996) and ASMOOTH (Ebeling et al. 2006). In the present adaptation, we smooth the inverted image not the observed image.

Our adaptive smoothing is performed by multiplying a multi-scale smoothing kernel,  $\mathcal{K}(\sigma, \vec{r})$  tile-by-tile over the inverted image plane. The relation between the input image  $s'(\vec{r})$  and the smoothed image  $s^*(\vec{r})$  is represented by

$$\vec{s}^*(\vec{r}) = \int s'(\vec{r}') \mathcal{K}(\sigma(\vec{r}); \vec{r}' - \vec{r}) d\vec{r}' \quad (6)$$

We here note that the width  $\sigma(\vec{r})$  is defined in the smoothed image space  $\vec{r}$ , not in the input image space  $\vec{r}'$ .

We use a Gaussian kernel. The smoothing matrix ( $N \times N$  dimension) for pixelized image is

$$F = \{\mathcal{K}(\sigma(\vec{r}_i), \vec{r}_j - \vec{r}_i)\}_{i=1\dots N, j=1\dots N} \quad (7)$$

$$= \left\{ \frac{1}{2\pi\sigma_i^2} \exp\left(-\frac{|\vec{r}_j - \vec{r}_i|^2}{2\sigma_i^2}\right) \right\}_{i=1\dots N, j=1\dots N} \quad (8)$$

The smoothed image  $\vec{s}^*$  and the noise image  $\vec{n}^*$  are represented by

$$\vec{s}^* = FP^{-1}\vec{d} = T\vec{d} \quad (9)$$

$$\vec{n}^* = FP^{-1}\vec{n} = T\vec{n} \quad (10)$$

where  $FP^{-1} = T = \{t_{ij}\}_{i=1\dots N, j=1\dots N}$ . The signal-to-noise ratio at each pixel  $\{SNR_i\}_{i=1\dots N}$  is then,

$$SNR_i = \frac{s_i^*}{n_i^*} = \frac{T\vec{d}}{T\vec{n}} = \frac{\sum_j t_{ij}d_j}{\sum_j t_{ij}n_j} \quad (11)$$

When Poisson noise is dominant and  $d_i$  is large,  $n_i = \sqrt{d_i}$ . Since the Poisson noise of photon counts at each pixel can be regarded as mutually independent, the equation (11) is reduced to the following equation.

$$SNR_i = \frac{\sum_j t_{ij}d_j}{\sqrt{\sum_j (t_{ij}n_j)^2}} = \frac{\sum_j t_{ij}d_j}{\sqrt{\sum_j t_{ij}^2 d_j}} \quad (12)$$

### 2.3. Search for Optimal Smoothing Scales

Our strategy is to find a set of smoothing widths  $\{\sigma_i\}_{i=1\dots N}$  so that the signal-to-noise ratio  $\{SNR_i\}_{i=1\dots N}$  agree with a given preset value  $SNR_{\text{opt}}$  at every pixel on the image. We developed a deconvolution program to search for an optimum iteratively. A similar method has been used in ASMOOTH (Ebeling et al. 2006). The program starts to test smoothing widths  $\{\sigma_i\}_{i=1\dots N}$  from an initial minimum value. The larger the smoothing width is, the lower the spatial resolution of the inverted image will be. The program increases each of  $\{\sigma_i\}_{i=1\dots N}$  step by step, then stops to increase  $\sigma_i$  when  $SNR_i$  reaches the preset desired value. This step is repeated until  $SNR_i$  reaches the desired value for all pixels or  $\sigma_i$  reaches a preset maximum value.

The deconvolution program takes four parameters: the desired signal-to-noise ratio  $SNR_{\text{opt}}$ , the minimum smoothing scale  $\sigma_{\text{min}}$ , the maximum smoothing scale  $\sigma_{\text{max}}$ , and the increment for each iterative step  $\Delta\sigma$ . Among the four parameters, the deconvolution result is sensitive only to the signal-to-noise ratio  $SNR_{\text{opt}}$ . The minimum scale  $\sigma_{\text{min}}$  and the increment for each step  $\Delta\sigma$  are chosen to be smaller than 1 tile size of the input image ( $= 6''$ ) to achieve

the maximum resolution. The maximum scale  $\sigma_{\max}$  is chosen as large as the standard deviation of the PSF ( $\simeq 30''$ ). We use the parameter values,  $SNR_{\text{opt}} = 4.0$ ,  $\sigma_{\min} = 2''.4$ ,  $\sigma_{\max} = 24''$ ,  $\Delta\sigma = 1''.4$  in the tests of the deconvolution method in section 5.

### 3. XIS Data

We used Suzaku archival data released via the pipeline processing version 1.2.2.3. The data has been processed using the HEADAS software version 6.1.2 released from the NASA/GSFC Guest Observer Facility. We extracted raw XIS images from the XIS event data screened by the standard screening procedure.

#### 3.1. Correction for XRT Alignment Error

The pointing direction of the Suzaku's XRTs has been found to wobble by  $\sim 40''$  roughly synchronized with the 96-minute orbital motion of the spacecraft (Serlemitsos et al. 2007). This wobbling is now understood as due to thermal distortion. The distortion is introduced when the side panel #7 on which the star trackers and the gyroscopes are mounted, is illuminated by sun-lit Earth. (Serlemitsos et al. 2007). Software to correct for the alignment error is now available (Uchiyama et al. 2008). However, it was not available at the time of this work and we corrected for this error using X-ray point sources in the data.

The corrections are done in two steps. Firstly, data was divided into 500-second intervals and the position of a bright point source is monitored for each interval. Figure 1 shows the time variation of the source position in the observed Cen A data in the initial performance verification phase. The periodicity of the 96-minute period is seen clearly. The images for 500-second intervals were shifted so that the Cen A align to one position. Figure 2 shows the XIS-0 image of Cen A before and after the pointing-error correction. The image is sharpened by the pointing-error correction.

### 4. Point Spread Function Modeling

Four XRTs have different complex position-dependent PSFs and they were calibrated on ground (Itoh et al. 2004a; Itoh et al. 2004b; Misaki et al. 2004). The PSFs observed in orbit are different from those measured on the ground because of absence of gravity in orbit. Hence, the PSF models made on the ground calibration have to be modified for the present application.

We constructed two PSF models: one based on the ray-tracing simulator, *xissim*, which we call the *xissim* PSF and the other on the observed Cen A image, the observed PSF. The *xissim* PSF implements the position-dependence in the entire image area. However *xissim* is based on the ground calibration and does not agree with the in-orbit point source images. On the other hand, the observed PSF is available only near the optical axis of each XIS. We combined the two PSF models when possible: the observed PSF for the central region within  $6'$  from the optical axis and the *xissim* PSF for the outer region.

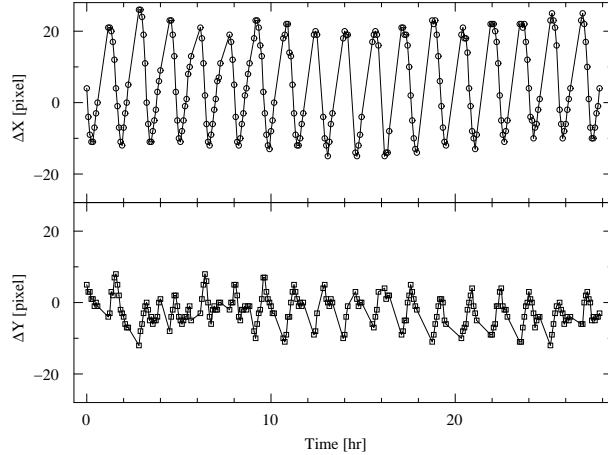


**Fig. 1.** Time variation of the position of Cen A in the XIS-0 image during observation started at 2005-08-19 05:55:00 (UTC). The CCD pixel width is  $1''.04$ .

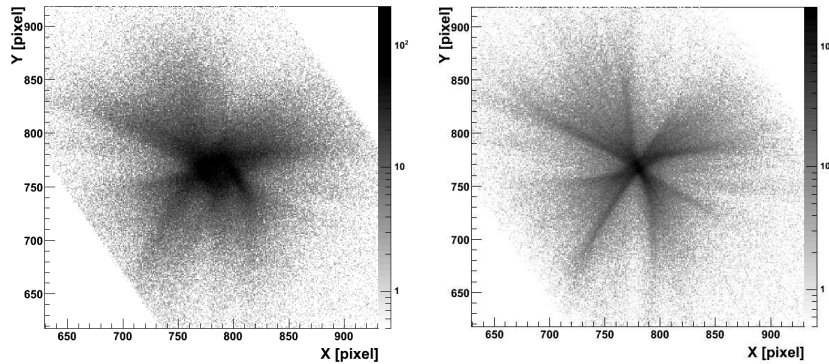


**Fig. 2.** XIS-0 images of Cen A in 0.5–10 keV band before the XRT alignment-error correction (*left*) and after the correction (*right*).

#### 4.1. *Xissim* PSF

The XRT ray-tracing library, *xissim*, is included in Suzaku FTOOLS in the HEADAS software package (Ishisaki et al. 2007). We simulated PSF images for  $16 \times 16$  source locations,

$$(DETX, DETY) = (32 + 64 \times i, 32 + 64 \times j) \quad (0 \leq i < 16, 0 \leq j < 16) \quad (13)$$

where each PSF represents a  $1'.1 \times 1'.1$  segment on the  $17'.7 \times 17'.7$  XIS image area. We assumed that the four quadrants of each XRT mirror are identical and each quadrant has a mirror-symmetry relative to the median angle of the quadrant. This means that the position dependence of PSF has four-fold axis-symmetry around the optical axis of the XRT and each quadrant has internal mirror symmetry. The position dependence of PSF has been simulated in the  $1/8$  triangular region of the square XIS FOV. The left panel of figure 3 shows the simulated position dependence of PSF.

The simulated PSF images have then been fitted with an analytic model function. Figure

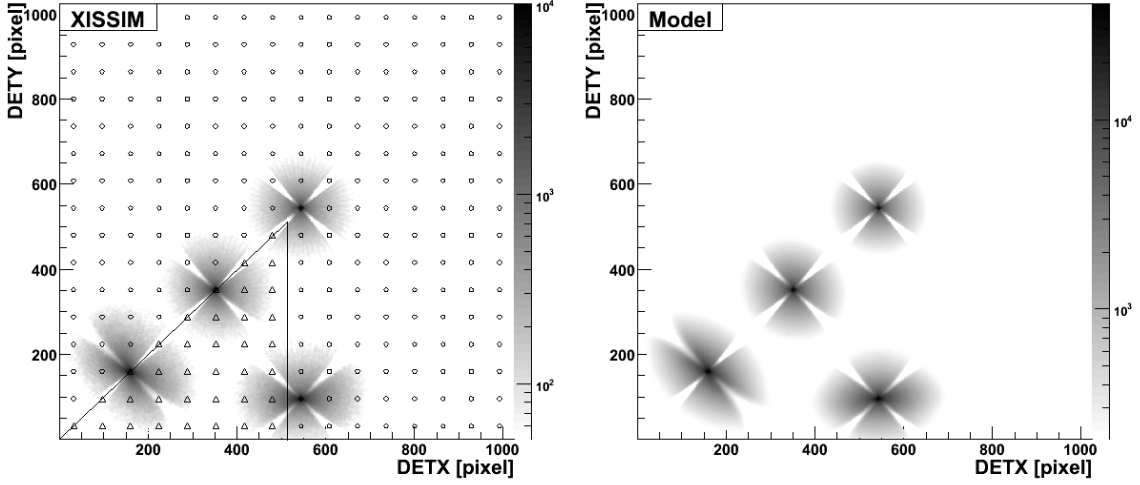


**Fig. 3.** (Left): PSF samples generated by XRT/XIS simulator, *xissim*. Open triangles are positions at which PSFs are simulated. Open circles show the grid points where PSF can be taken from the symmetric point in the triangle. (Right): PSFs generated with our Xissim PSF model. Gray contour colors are spaced logarithmically in the both figures.

4 illustrates parameters used in the PSF model: the X-ray source position  $(\theta, \phi)$ , the detected photon position  $(\rho, \psi)$ , and coordinates for the mirror quadrant boundaries by  $(\alpha, \beta)$ . The function of the *xissim* PSF,  $PSF_{\text{xissim}}(\theta, \phi; \rho, \psi)$ , consists of a central peak profile represented by three exponential distributions,  $p(\theta, \phi; \rho, \psi)$ . The sensitivity gaps at the boundaries of the mirror quadrant are represented by  $q(\theta, \phi; \rho, \psi)$ . They take the following formulae:

$$PSF_{\text{xissim}}(\theta, \phi; \rho, \psi) = p(\theta, \phi; \rho, \psi)q(\theta, \phi; \alpha, \beta) \quad (14)$$

$$p(\theta, \phi; \rho, \psi) = \sum_{i=1,2,3} c_i \exp\left(\frac{-\rho}{\sqrt{a_i^2 \cos^2 \psi + b_i^2 \sin^2 \psi}}\right) \quad (15)$$

$$q(\theta, \phi; \alpha, \beta) = \begin{cases} 1 & (|\alpha| \leq k_1, |\beta| \leq h_1) \\ \left[1 + \exp\left(\frac{k_2(|\alpha| - k_1) - |\beta|}{k_3(|\alpha| - k_1) + k_4}\right)\right]^{-1} & (|\alpha| \geq |\beta|) \\ \left[1 + \exp\left(\frac{h_2(|\beta| - h_1) - |\alpha|}{h_3(|\beta| - h_1) + h_4}\right)\right]^{-1} & (|\alpha| < |\beta|) \end{cases} \quad (16)$$

Each simulated PSF at  $(\theta, \phi)$  is fitted to obtain the 17 parameters,  $\{a_i, b_i, c_i\}_{i=1,2,3}$  and  $\{k_i, h_i\}_{i=1,2,3,4}$ . The right panel of figure 3 shows the fitted PSF. We calculate the PSF for arbitrary position by interpolating from the simulated PSFs at the grid points.

#### 4.2. Validation of *xissim* PSF

We have validated the *xissim* PSF model by comparing actual observed image of Cen A in 2–10 keV band. The central X-ray source is known to be point-like in the energy band



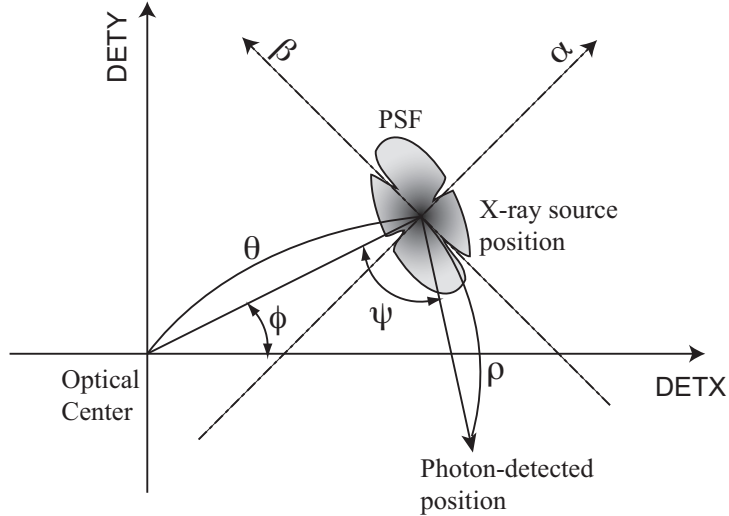


Fig. 4. Coordinate definition used in PSF modeling.

(Evans et al. 2004; Markowitz et al. 2007).

Figure 5 shows the Cen A images taken with the four XISs after the XRT alignment-error correction, and the model PSF. The observed Cen A image is similar to the PSF model, but there are apparent differences. Figure 6 shows the radial profiles of the observed Cen A images and the xissim PSF model averaged over the  $360^\circ$  azimuthal angle and the azimuthal profiles of an annulus between radii  $r = 40$  pixel and  $r = 60$  pixel. The azimuthally averaged radial profile of the Cen A images agree well with the model PSF except for the central core of radius  $r < 5''$ . On the other hand, the azimuthal profiles of the Cen A images are significantly different from the model PSF, reflecting the complicated asymmetric profiles of the real XRT-XIS system.

Among the Cen A images observed by the four XISs, that of the XIS-1 came closest to the model PSF. Hence, we have decided to use XIS-1 to test the image deconvolution method in section 5.

#### 4.3. Observed PSF

We made another PSF model out of the observed Cen A image, and call it the observed PSF. We plot radial profiles of the Cen A image for several azimuth angles in the left panel of figure 7. These profiles are fitted with a model functions consisting of two exponentials. The PSF model is formulated on the best-fit radial profiles. The obtained observed PSF model is shown in the right panel of figure 7.

The archived data of Cen A were taken in one pointing and hence position dependence of PSF could not be extracted. Because of this, we use the observed PSF only for the central region of the XIS FOV in the deconvolution analyses described below.

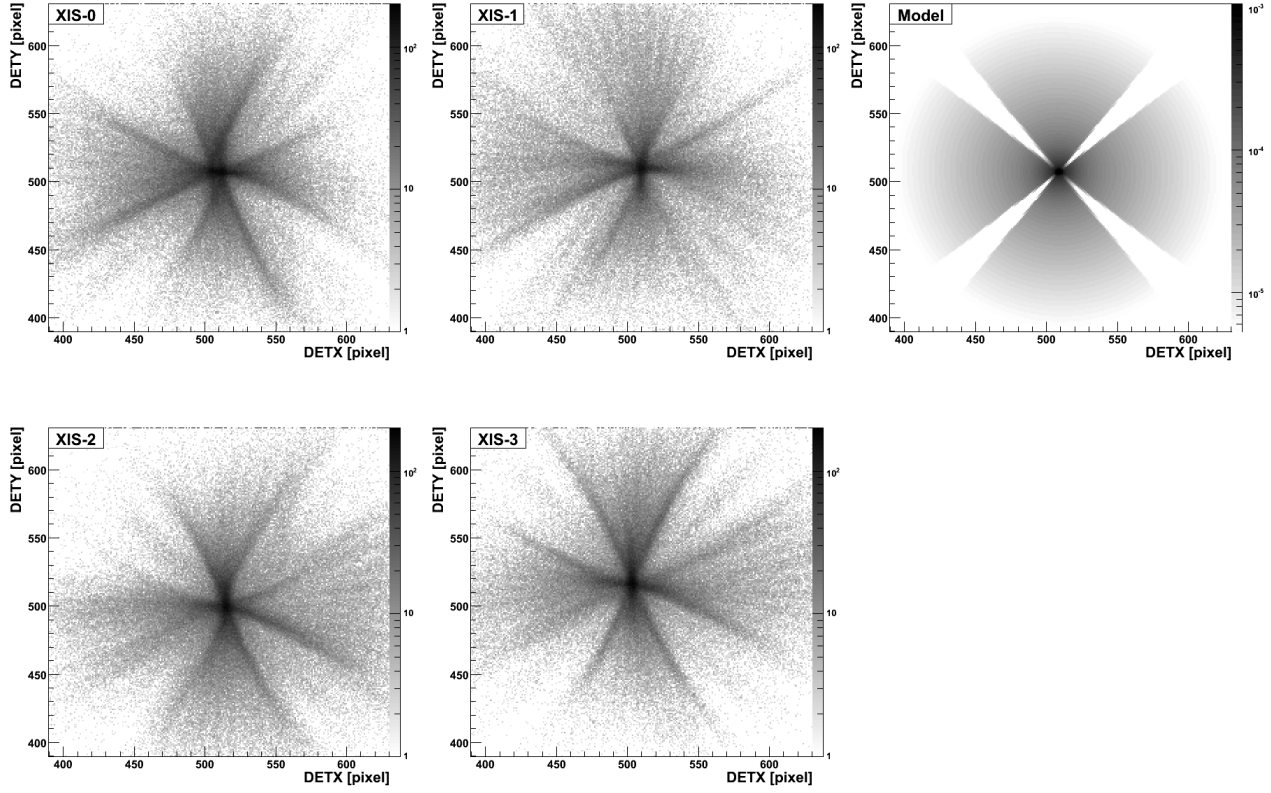


**Fig. 5.** Four XIS images of Cen A in 2–10 keV band and xissim PSF. The gray contour colors are spaced logarithmically.

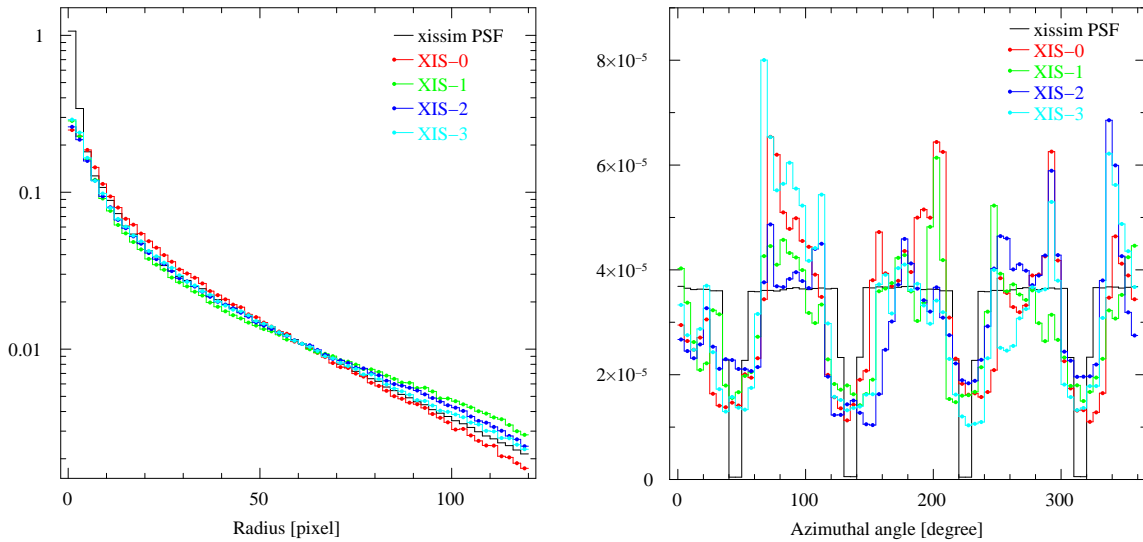


**Fig. 6.** (Left): Radial profiles of xissim PSF and images of Cen A in 2–10 keV observed by each XIS detector. All profiles are normalized to 0.01 at a radius of 60 pixel. (Right): Azimuthal profiles extracted from annulus between radii  $r = 40''$  and  $r = 60''$ .

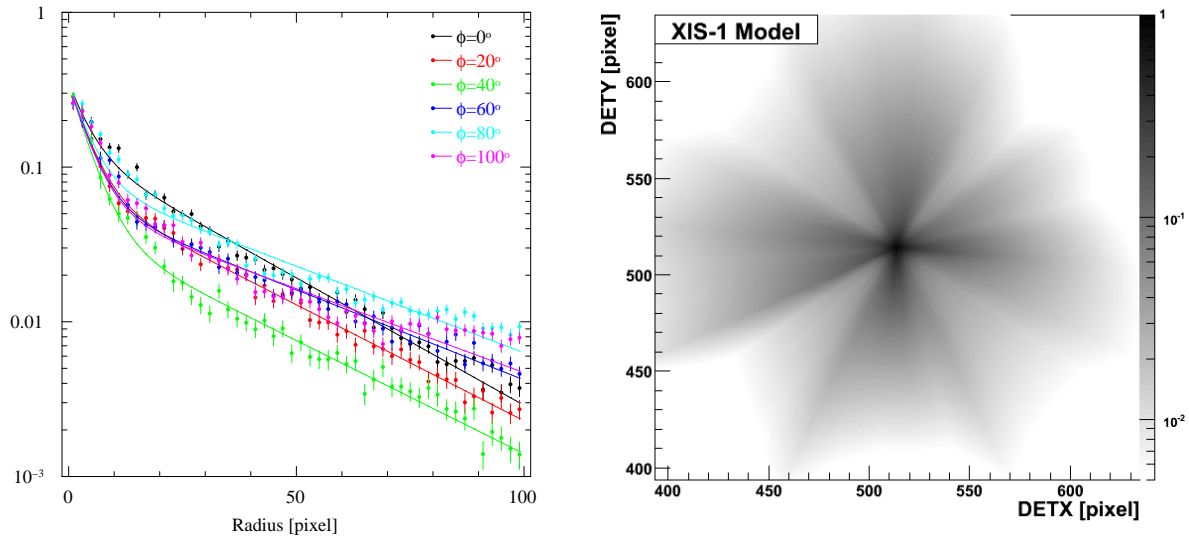


**Fig. 7.** (Left): Radial profiles of XIS-1 Cen A image in 2–10 keV band with statistical errors and their best-fit model functions (solid lines) for various azimuthal angles. (Right): Observed PSF model for central region of XIS-1 image.

## 5. Application to XIS images

We have applied the present deconvolution method to simulated XIS images as well as to observed images in the Suzaku archival data. We have chosen Cen A, PSR B1509-58 and RCW 89 as targets because they include both a bright point source and extended emissions and also because there are Chandra observations of the same regions. The bright point sources serve to correct for the XRT pointing error as has been described in section 3.1. The images of Chandra ACIS are used to evaluate the fidelity of the deconvolved images.

### 5.1. Deconvolution of Images

The deconvolution program is developed on a standard Linux machine in the C program language using BLAS<sup>1</sup>/ LAPACK<sup>2</sup> linear algebra program libraries (Anderson et al. 1999) customized by ATLAS project (Whaley et al. 2001).

The deconvolution of XIS images proceeds in the following steps.

1. Extract a region of interest from the entire XIS image ( $1024 \times 1024$  pixels covering area of  $17'.8 \times 17'.8$ ) and make a  $64 \times 64$  tiled image where each tile is combination of  $6 \times 6$  XIS CCD pixels (each CCD pixel covers  $6''.3 \times 6''.3$ ). For RCW 89, the tile size has been set larger to cover  $8 \times 8$  CCD pixels because number of photon per tile was lower.
2. Make a response function based on the two PSF models. The PSF is normalized to 1.0 so

<sup>1</sup> <http://www.netlib.org/blas/>

<sup>2</sup> <http://www.netlib.org/lapack/>

that the number of photons is preserved. We employed the observed PSF model for the region within  $6'$  from the XRT optical axis. Exception is RCW 89. The xissim PSF model was used for RCW 89.

3. Calculate the inverse of the response matrix.
4. Multiply the inverse response matrix with the tiled image
5. Smooth the response-inverted image adaptively. The adaptive smoothing takes a signal-to-noise ratio,  $SNR_{\text{opt}}$  as a parameter. We set  $SNR_{\text{opt}} = 4.0$  as described in section 2.3 for all the examples described below.

### 5.2. Test with Simulated Images

We have tested the fidelity of the present deconvolution method using simulated XIS-1 images. The simulated image consists of three point sources and an extended source as shown in figure 8. The surface brightness of the extended emission is represented by a simple  $\beta$  model:

$$S(r) = S_0 \left\{ 1 + (r/r_c)^2 \right\}^{-3\beta+0.5}, \quad (17)$$

where the critical radius is set to  $r_c = 30''$  and  $\beta$  to 0.5. Relative fluxes of three point sources and extended emission are set at  $4:2:1:40$ . To study how fidelity depends on photon statistics, we have deconvolved three images containing total signal photons of 20,000, 100,000, and 500,000 and background photons expected for nominal blank-sky in a 50-ks exposure (Mitsuda et al. 2007). These images are then compared with images deconvolved by a Richardson-Lucy method with 100 iterations in figure 8.

One can see that the Richardson-Lucy method adds photons to high points in Poisson fluctuation noise and depletes photons from low points in the fluctuation. Our method, on the other hand, smooths out the fluctuation below the predetermined signal-to-noise ratio while reproducing the three point sources and the extended source well. Such noise filter can be added to the Richardson-Lucy method to suppress artifacts but the filtering strategy is strongly coupled with the number of iteration. We note that the raw image of 100,000 photons at the middle row in Figure 8 has about  $\sim 50$  signal photons and  $\sim 3$  noise photons per tile in average within the critical radius  $r_c = 30''$ .

### 5.3. Cen A

The data of Cen A are divided into two energy bands,  $> 3$  keV and  $< 3$  keV, and the two images are deconvolved separately. In the hard band, the flux of Cen A is known to be dominated by the central point source (Evans et al. 2004; Markowitz et al. 2007). In the soft band, an extended jet profile with a scale of  $30''$ – $180''$  has been observed by Chandra (Kraft et al. 2002; Kataoka et al. 2006).

#### 5.3.1. Hard band: 3–10 keV

Figure 9 shows the observed image of XIS-1 in 3-10 keV band, its deconvolved image, and the Chandra ACIS image rebinned to the tile size. We have also convolved the Chandra

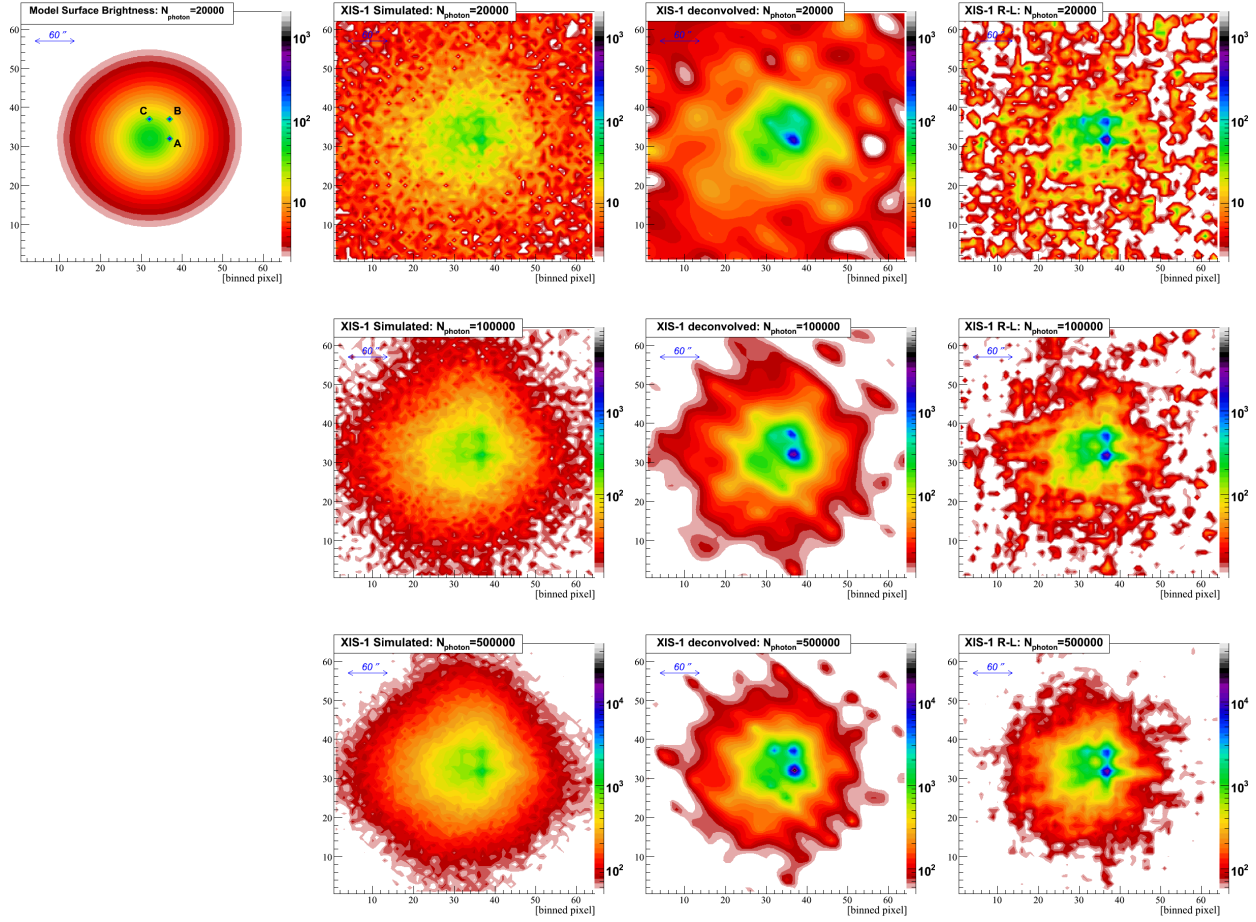


**Fig. 8.** Deconvolution of simulated XIS-1 images. (Left) Model image consists of three point sources and an extended emission. Relative fluxes of the three point sources (A, B, C) and extended emission are 4 : 2 : 1 : 40. (Center left) Simulated XIS-1 images with photon counts of 20,000, 100,000, 500,000 from top to bottom. Background photons with Poisson distribution expected for a nominal blank-sky in a 50-ks exposure are included. (Center right) Deconvolved XIS-1 images with 20,000, 100,000, and 500,000 photons from top to bottom by the present method. (Right) Deconvolved XIS-1 images by a Richardson-Lucy method after 100 iterations.

image with the XIS-1 PSF and shown in the top right panel. We note that the Chandra ACIS image is distorted by the pile-up effect at the Cen-A nucleus and the one shown in figure 9 has been corrected for the distortion by using the Suzaku XIS image.

We have studied the deconvolved Suzaku image by slicing it along the 3 blue dash-dot lines drawn at  $\phi = -33^\circ, 0^\circ$ , and  $33^\circ$  from the Right Ascension axis crossing the Cen A core in figure 9. The surface brightness profiles are compared with those of the XIS-1 raw image and the Chandra ACIS image in figure 10. The surface brightness was calculated by assuming a power-law spectrum with photon index  $\Gamma = 1.8$  (Markowitz et al. 2007). The vertical scale of the XIS-1 raw image was normalized at the peak to the deconvolved image.

In the deconvolved image, the large wings extending over  $\sim 120''$  in the raw images are drastically reduced. The width of the central peak in the deconvolved image is wider by  $12'' - 24''$  than the ACIS image. This is interpreted that the spatial resolution has been improved to  $12'' - 24''$  by deconvolution but not better. The spatial resolution depends on the azimuth angle: It is the worst at  $\phi = 33^\circ$ , which corresponds to the direction along which the PSF is extended. We find two artifact peaks in the region  $50'' - 100''$  away from the peak in all three profiles at about  $1/50$  of the peak surface brightness. This shows limitation of the present deconvolution method. With the present modeling of the XIS PSF, our deconvolution reconstructs the image down to about 1:50. A third exponential component with a wider wing may be required to improve the dynamic range.

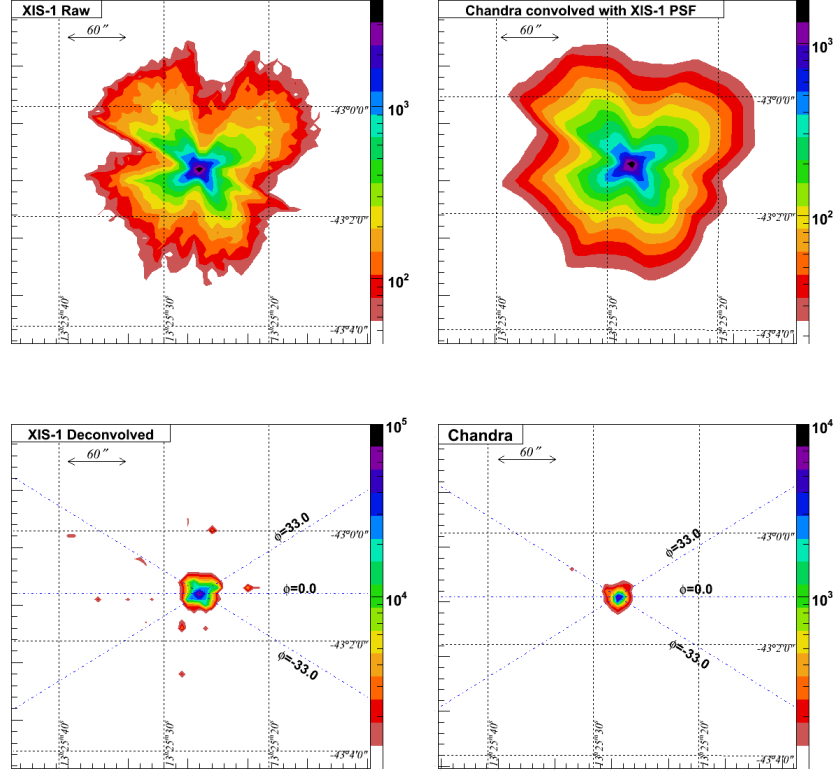
### 5.3.2. *Soft band: 0.5–3 keV*

Figure 11 shows the observed image of XIS-1 in 0.5-3 keV band, the deconvolved image, and the rebinned Chandra ACIS image. The convolved ACIS image with the XIS-1 PSF is also shown in the top right panel. The pile-up effect at the nucleus of Cen A in the ACIS image is corrected from the flux measured by the XIS. Our deconvolution reconstructs the bright blob “B” but not the blob “C” in the jet.

Figure 12 shows the cross-section profiles of the XIS-1 raw, deconvolved, and ACIS images sliced along the direction to the north-east jet (a dash-dot blue line in figure 11). Here, the surface brightness is calculated assuming a power-law spectrum with photon index  $\Gamma = 1.3$  (Markowitz et al. 2007). The profile around peak is well restored in the deconvolved image with a spatial resolution of  $20''$ . The restored image is consistent with that by Chandra if we take the pile-up effect in the Chandra image into account.

### 5.4. *PSR B1509-58 and RCW 89*

The observed region of PSR B1509-58 includes a bright point source PSR B1509-58 and an extended source RCW 89 (Yatsu et al. 2005; DeLaney et al. 2006). Figure 13 shows the overall image by XIS-1. The hard band image exhibits only one point source, PSR B1509-58, and no extended emission. The image in the soft band consists of complex extended emissions as shown in the next subsection.



**Fig. 9.** XIS-1 raw image (*top left*), convolved Chandra ACIS image with XIS-1 PSF (*top right*), XIS-1 deconvolved image (*bottom left*), and Chandra ACIS image (*bottom right*) of Cen A in 3–10 keV. All images are binned with a same unit tile size of  $\sim 6'' \times 6''$ . Contour colors are spaced logarithmically. Notice that the Chandra ACIS image suffers from the pile-up effect at the nucleus of Cen A (the brightest point). Blue dash-dot lines indicate the sliced directions in figure 10.

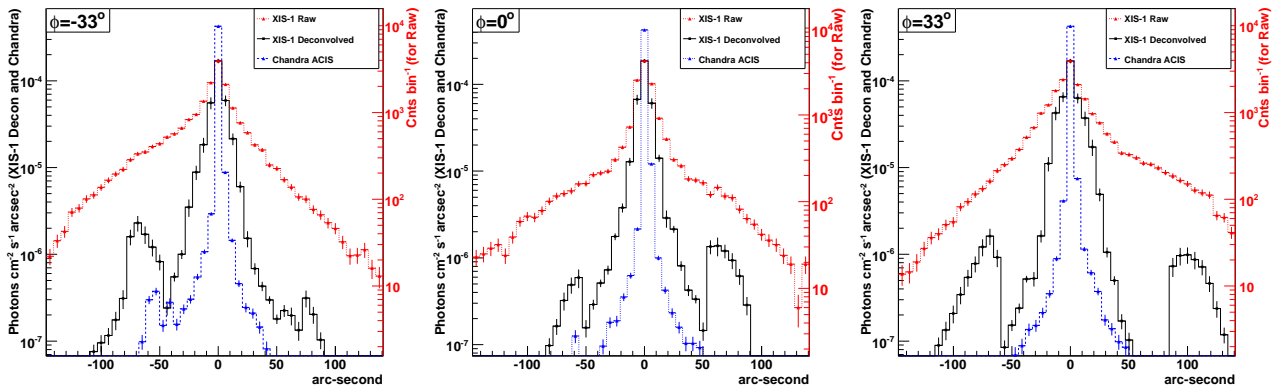


**Fig. 10.** Cross-section profiles of the XIS-1 raw image (red dot) deconvolved image (black solid) and Chandra ACIS image (blue dash) of Cen A in 3–10 keV band, sliced along the blue dash-dot lines in figure 9. Error bars represent  $1\text{-}\sigma$  photon-statistics uncertainties. The vertical scale of the raw image is normalized by the peak value to the deconvolved image. Notice that the pile-up effect at the peak of the Chandra ACIS image (one pixel at the center) is corrected.

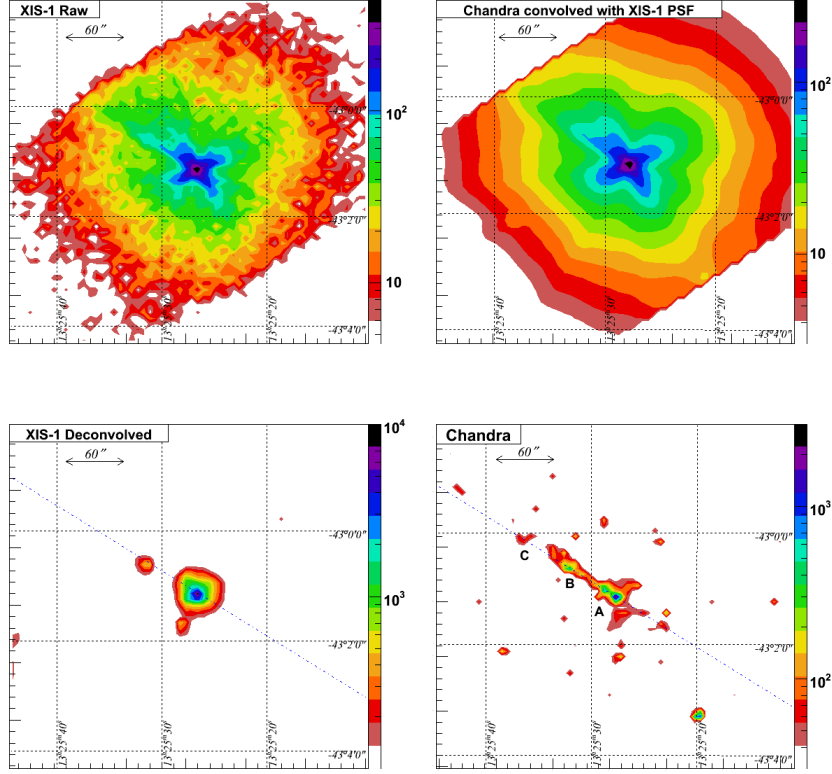


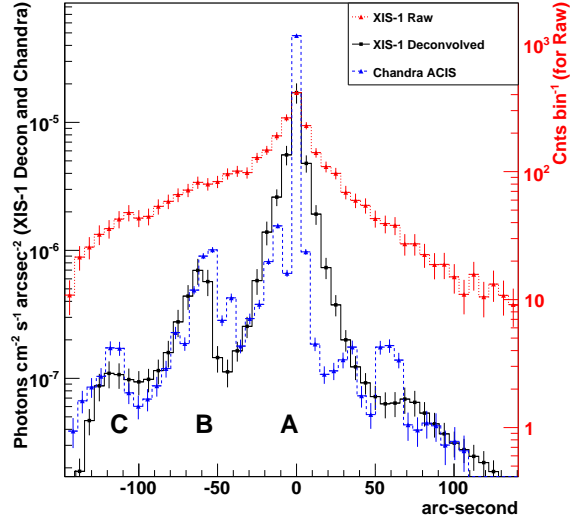
**Fig. 11.** XIS-1 raw image (*top left*), convolved Chandra ACIS image with XIS-1 PSF (*top right*), XIS-1 deconvolved image (*bottom left*), and Chandra ACIS image (*bottom right*) of Cen A in 0.5–3 keV band. All images are binned with a same unit tile size of  $\sim 6'' \times 6''$ . In images of XIS-1, the blank areas at the top left and the bottom right are not covered by clocked CCD window in this observation. Note that the peak of the Chandra ACIS image (one pixel at the center) suffering from a pile-up effect has been corrected using the flux measured by the Suzaku XIS. The blue dash-dot lines on the XIS-1 deconvolved image and the Chandra image indicate the sliced direction in Figure 12. The labels “A”, “B”, “C” in the Chandra image identify the peaks.

#### 5.4.1. PSR B1509-58: 0.5–3 keV

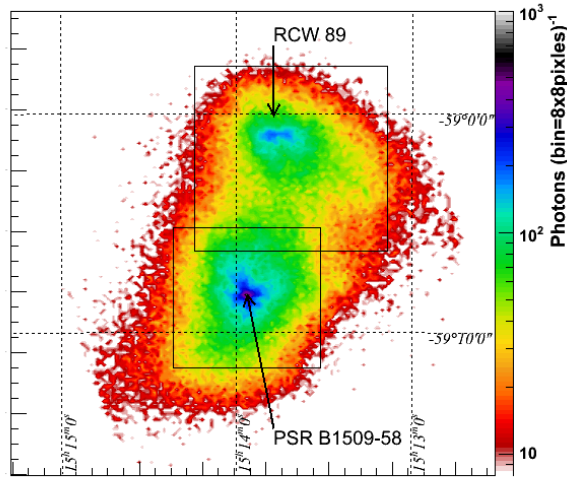
The raw image of the region including PSR B1509-58 and RCW 89 is shown in figure 13. The image includes interesting extended emissions and a point source, and can be viewed as a typical target for our image deconvolution program.

Figure 14 shows the raw XIS-1 image and the deconvolved image in the 0.5–3 keV band, and the Chandra ACIS image with that convolved with the XIS-1 PSF. These cross-section profiles along the Right Ascension axis are also shown. The surface brightness was calculated assuming a power-law spectrum with photon index  $\Gamma = 1.8$ . The Chandra image suffers from the pile-up effect at the position of PSR B1509-58. The sliced surface brightness profile of the deconvolved image is consistent with the Chandra image if the pixel saturation is corrected using the XIS-1 image.





**Fig. 12.** Cross-section profiles of XIS-1 raw image (red dot) and deconvolved image (black solid) and Chandra ACIS image (blue dash) of Cen A in 0.5-3 keV sliced along the direction of the jet (blue dash-dot lines in figure 11). Error bars represent  $1\text{-}\sigma$  photon-statistics uncertainties. The vertical scale of XIS-1 raw data is normalized at the peak value to the deconvolved image. The peak of the Cen-A nucleus in the Chandra profile has been corrected for the pile-up effect. The labels “A”, “B”, “C” indicate the peaks in figure 11.



**Fig. 13.** XIS-1 overall raw image of PSR B1509-58 and RCW 89 in 0.5–3 keV band. Solid boxes represent the regions of which images are applied to the deconvolution analysis.

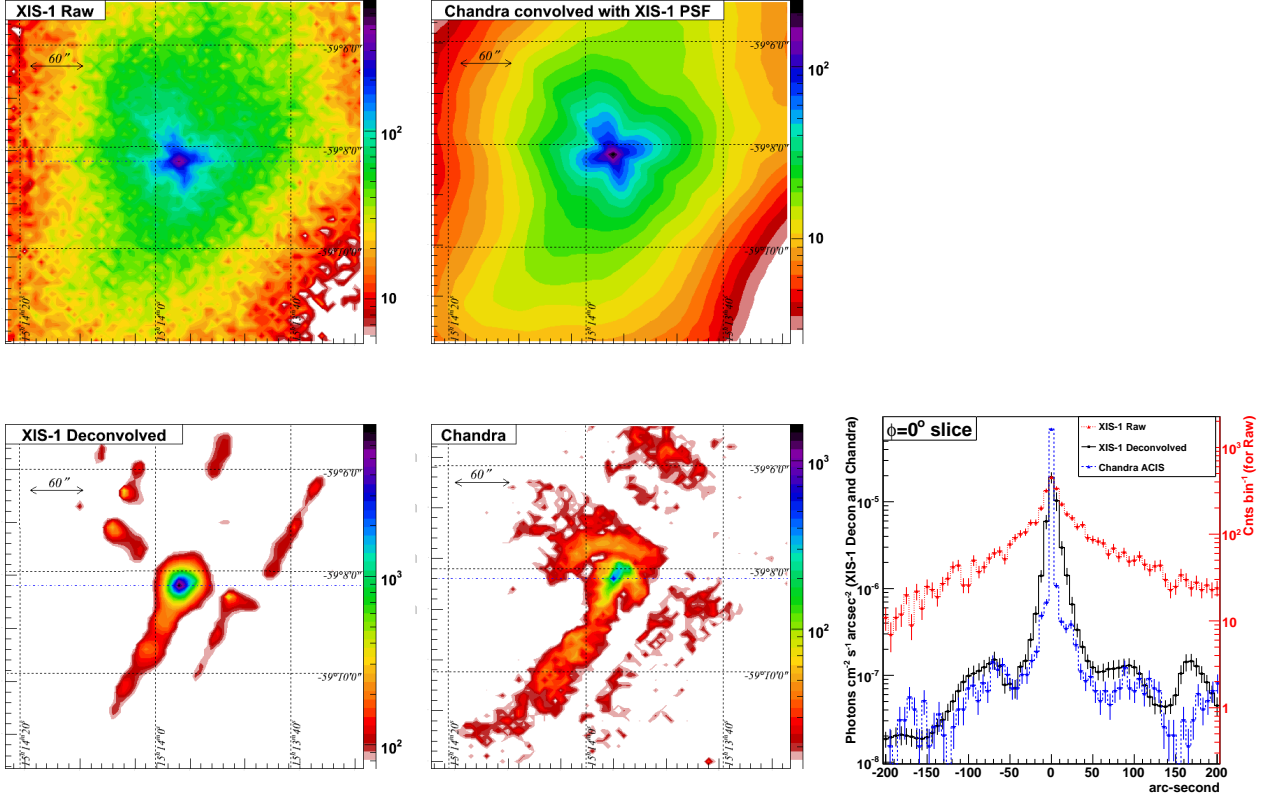


**Fig. 14.** PSR B1509-58 region: XIS-1 raw image (*top left*), convolved Chandra ACIS image with XIS-1 PSF (*top center*), XIS-1 0.5-3 keV deconvolved image (*bottom left*), Chandra ACIS 0.5-3 keV image (*bottom center*), and cross-section profiles sliced along Right Ascension (blue dash-dot lines in the images) (*bottom right*). Both XIS-1 and Chandra ACIS images are binned with a same tile size of  $\sim 6'' \times 6''$ . A pixel of the central core of PSR B1509-58 in the Chandra image is corrected for the pile-up effect. Error bars in cross-section profiles represent  $1-\sigma$  photon-statistics uncertainties.

The jet-like structure extending from the pulsar is restored in the deconvolved image. However other extended features around the pulsar are missed or incorrectly restored. Their surface brightness is lower than  $1/50$  of the peak value, or below the dynamic range of this deconvolution method.

#### 5.4.2. RCW 89: 0.5–3 keV

Figure 15 shows the raw XIS-1 image and the deconvolved image of RCW 89 in the 0.5–3 keV band, and the Chandra ACIS image with that convolved with the XIS-1 PSF. These cross-section profiles along the Right Ascension axis are also shown. For this source,  $8 \times 8$  raw pixels were combined to one tile to secure high numbers of photons per tile. The xissim PSF model was used in the response matrix inversion because the image area extended larger than  $6'$  from the XRT optical axis. The surface brightness is calculated assuming a power-law spectrum with photon index  $\Gamma = 1.8$ . The extended bright region of scale greater than  $\sim 20''$  in the upper part of the image has been reproduced well in the deconvolved XIS-1 image but

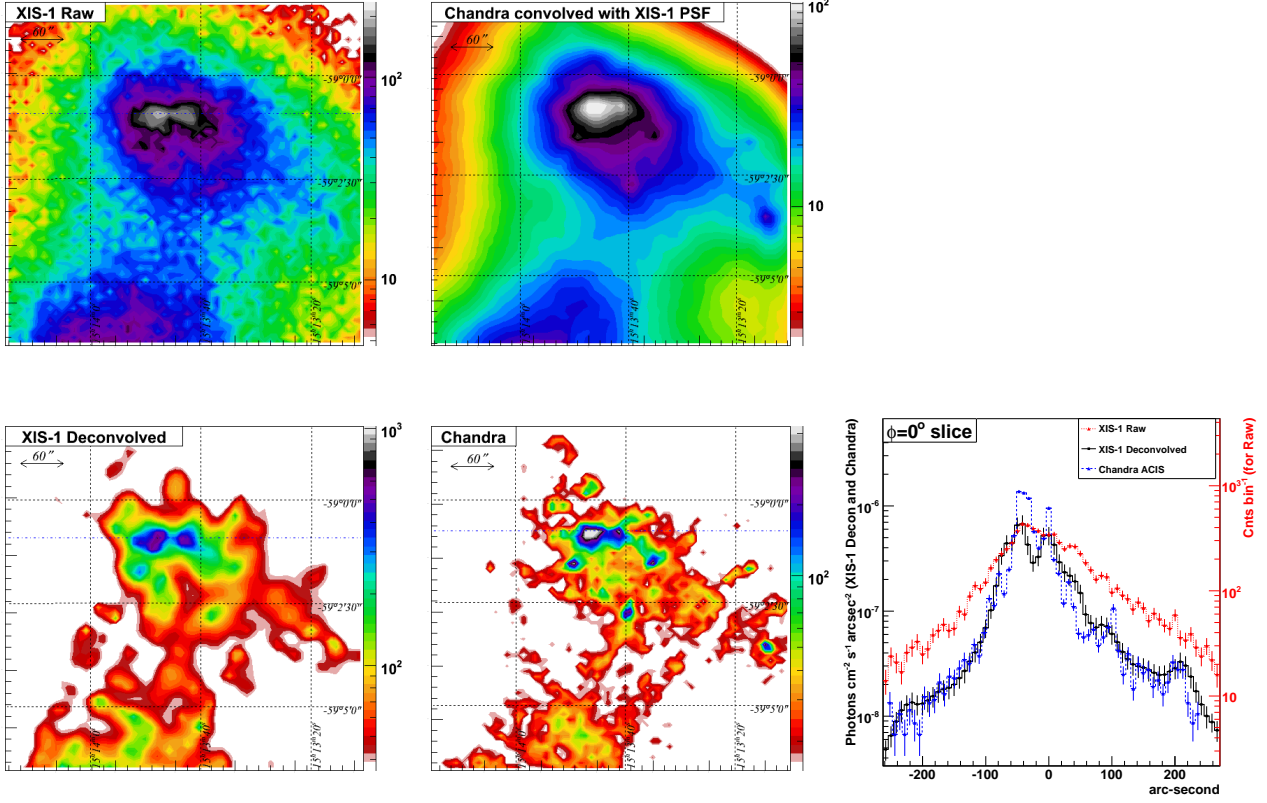


**Fig. 15.** RCW 89 region: XIS-1 raw image (*top left*), convolved Chandra ACIS image with XIS-1 PSF (*top center*), XIS-1 0.5-3 keV deconvolved image (*bottom left*), Chandra ACIS 0.5-3 keV image (*bottom center*), and cross-section profiles sliced along Right Ascension (blue dash-dot lines in the images) (*bottom right*). Both XIS-1 and Chandra images are binned with a same tile size of  $\sim 8'' \times 8''$ . Error bars in peak cross-section profiles represent  $1-\sigma$  photon-statistics uncertainties.

positions of narrower high points do not agree with those in the Chandra image. We interpret this due both to the inaccuracy of the xissim PSF model and to the limited angular resolution of  $\sim 20''$ . Within these limitations, the deconvolution method has reproduced the prominent shell-like structure in the upper part.

## 6. Conclusion and Future Prospect

We have developed an image deconvolution method for the Suzaku XIS based on response matrix inversion and adaptive smoothing. The method has been tested with two XIS-1 images both containing extended sources and one prominent point source: Cen A and PSR B1509-58/RCW 89. By comparing the deconvolved images with the corresponding Chandra ACIS images, we conclude that spatial resolution has been restored to  $\sim 20''$  to a brightness level around 1/50 of the brightest tile in the image.

Recent X-ray instruments including Suzaku are finding complex morphology of thermal,

non-thermal and K-shell line emissions in many extended sources including young supernova remnants (SNRs) (e.g. Ueno et al. 2007), pulsar wind nebulae (PWNe) (e.g. Seward et al. 2006), the Galactic Center region (e.g. Koyama et al. 2007b; Koyama et al. 2007c; Koyama et al. 2007d), and galaxy clusters (e.g. Sanders et al. 2005). To understand such objects, the spatial resolution of Suzaku XIS has to be improved substantially. The present work provides a procedure for such improvement.

We plan to improve PSF modeling and incorporate the XRT alignment scheme developed by the Suzaku XIS team.

We are grateful to the Suzaku team and SLAC/KIPAC members for their support for the present work. Special thanks are due to Drs K. Makishima, K. Mitsuda, Y. Ogasaka, T. Takahashi, R. Blandford, S. Kahn, G. Madejski, and H. Tajima. We thank the anonymous referee for valuable comments. This work has been carried out under supports of the US Department of Energy contract to SLAC No. DE-AC3-76SF00515, Kavli Institute for Particle and Astrophysics and Cosmology (KIPAC) at Stanford University, and Japanese Ministry of Education, Culture, Sports, Science and Technology (MEXT), Grant-in-Aid No. 18340052.

## References

- Anderson, E. et al. 1999, LAPACK Users' Guide, Third Edition, Society for Industrial and Applied Mathematics), Philadelphia, PA
- DeLaney, T., Gaensler, B. M., Arons, J., & Pivovarov, M. J. 2006, ApJ, 640, 929
- Ebeling, H., White, D. A., & Rangarajan, F. V. N. 2006, MNRAS, 368, 65
- Evans, D. A., Kraft, R. P., Worrall, D. M., Hardcastle, M. J., Jones, C., Forman, W. R., & Murray, S. S. 2004, ApJ, 612, 786
- Huang, Z., & Sarazin, C. L. 1996, ApJ, 461, 622
- Hwang, U., & Gotthelf, E. V. 1997, ApJ, 475, 665
- Itoh, A., et al. 2004, Proc. SPIE, 5488, 93
- Itoh, K., et al. 2004, Proc. SPIE, 5488, 85
- Kataoka, J., Stawarz, L., Aharonian, F., Takahara, F., Ostrowski, M., & Edwards, P. G. 2006, ApJ, 641, 158
- Koyama, K., et al., 2007, PASJ, 59, 23
- Koyama, K., et al. 2007, PASJ, 59, 221
- Koyama, K., Uchiyama, H., Hyodo, Y., Matsumoto, H., Tsuru, T. G., Ozaki, M., Maeda, Y., & Murakami, H. 2007, PASJ, 59, 237
- Koyama, K., et al. 2007, PASJ, 59, 245
- Kraft, R. P., Forman, W. R., Jones, C., Murray, S. S., Hardcastle, M. J., & Worrall, D. M. 2002, ApJ, 569, 54
- Ishisaki, Y., et al. 2007, PASJ, 59, 113
- Lorenz, H., Richter, G. M., Capaccioli, M., & Longo, G. 1993, A&A, 277, 321

- Markowitz, A., et al. 2007, ArXiv e-prints, 704, arXiv:0704.3743
- Mitsuda, K., et al., 2007, PASJ, 59, 1
- Misaki, K., et al. 2004, Proc. SPIE, 5168, 294
- Puetter, R. C., Gosnell, T. R., & Yahil, A. 2005, ARA&A, 43, 139
- Sanders, J. S., Fabian, A. C., & Dunn, R. J. H. 2005, MNRAS, 360, 133
- Serlemitsos, P. J., et al., 2007, PASJ, 59, 9
- Seward, F. D., Tucker, W. H., & Fesen, R. A. 2006, ApJ, 652, 1277
- Starck, J. L., Pantin, E., & Murtagh, F. 2002, PASP, 114, 1051
- Uchiyama, Y., et al., 2008, PASJ, 60, 53
- Ueno, M., et al. 2007, PASJ, 59, 171
- Whaley R, Petitet A, & Dongarra J. 2001. “Automated Empirical Optimization of Software and the ATLAS Project” Parallel Computing 2001; 27(1-2):3-25.
- White, D. A., & Buote, D. A. 2000, MNRAS, 312, 649
- Yatsu, Y., Kawai, N., Kataoka, J., Kotani, T., Tamura, K., & Brinkmann, W. 2005, ApJ, 631, 312